CHEMISTRY OF MATERIALS

Article

pubs.acs.org/cm

Nanocomposites Containing Neutral Blue Emitting Cyclometalated Iridium(III) Emitters for Oxygen Sensing

Marta Marín-Suárez,[†] Basile F. E. Curchod,[§] Ivano Tavernelli,[§] Ursula Rothlisberger,[§] Rosario Scopelliti,[‡] Il Jung,[‡] Davide Di Censo,[‡] Michael Grätzel,[‡] Jorge Fernando Fernández-Sánchez,*[,†] Alberto Fernández-Gutiérrez,[†] Md. Khaja Nazeeruddin,[‡] and Etienne Baranoff*[,#,‡]

[†]Department of Analytical Chemistry, Faculty of Sciences, University of Granada, E-18071 Granada, Spain

[§]Laboratory of Computational Chemistry and Biochemistry, École Polytechnique Fédérale de Lausanne, CH-1015 Lausanne, Switzerland

[‡]Laboratory of Photonics and Interfaces, École Polytechnique Fédérale de Lausanne, CH-1015 Lausanne, Switzerland

[#]School of Chemistry, University of Birmingham, Edgbaston B15 2TT, England

Supporting Information

ABSTRACT: The behavior toward oxygen sensing of nanocomposites made of the aluminum oxide-hydroxide nanostructured solid support (AP200/19) and neutral blue emitting cyclometalated iridium(III) complexes was studied. The results are compared with the same dyes immobilized in polystyrene films. Since the photoluminescence of the complexes is totally quenched for oxygen concentrations just over 10%, these systems using the blue region of the visible spectrum are promising for oxygen detection at low concentration. In particular, dyes supported into the AP200/19 provide the best sensitivity to oxygen concentration, with the possibility to detect oxygen below 1% O_2 in gas (0.01 bar).

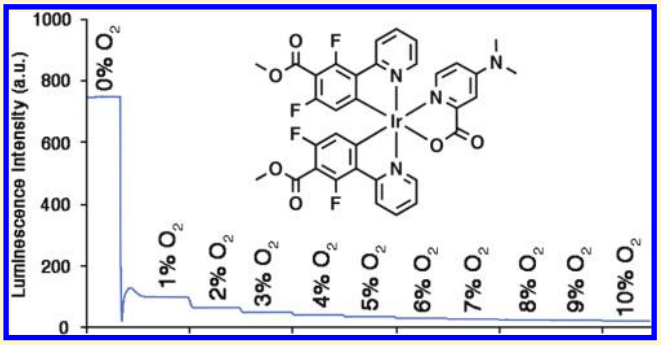

KEYWORDS: *cyclometalated iridium(III) complexes, phosphorescence, oxygen sensing, nanostructured films*

INTRODUCTION

Molecular oxygen plays an important role in life, since it is present in a variety of chemical reactions, not only as a reactant but also as a product. Although the detection of oxygen is well-known, in recent years optical oxygen sensing has attracted a lot of scientific attention as the dynamic quenching of the luminescence emission by oxygen has proved to be a very sensitive technique.[1] Optical oxygen sensors are based on luminescent dyes whose fluorescence or phosphorescence is quenched by molecular oxygen. This process takes advantage of the excited state properties of the dyes, and therefore, the effects of quenchers on intensity and decay time are nondestructive and fully reversible, allowing the continuous monitoring of oxygen.[1] Since nowadays it is paramount to develop methods for monitoring oxygen concentration in real time, optical sensors have become very popular in many fields related to industry, medicine, and environment.[2−9]

The quenching of an excited state by oxygen can occur through two mechanisms: electron transfer and energy transfer. In both cases, a long excited state lifetime will favor the process, enhancing the material oxygen sensing ability. In this respect, phosphorescent transition metal complexes are very appealing due to both their excited state lifetime on the microsecond time-scale and the triplet character of their emission, which increases the sensitivity to oxygen. Furthermore, cyclometalated iridium(III) complexes are attracting particular interest due to their generally high photoluminescence quantum yield and unique capability to have emission tuned over the entire visible spectrum.[10−12] Thus, in addition of their good chemical, photo- and electrochemical stability, cyclometalated iridium(III) complexes are an important class of dyes for oxygen sensing.[5,13−18] To date, all cyclometalated iridium(III) dyes used for oxygen sensing are red or green emitters. However, the ability of these complexes to have emission color tuned over the entire visible spectrum is attractive for developing oxygen sensitive blue dyes, with enhanced sensitivity, and quantum yield, which improves the efficiency of the devices. In addition, having optical sensors in the entire region of the visible spectrum would increase the sensor performance when natural red emitters are present in the media or in order to perform dual optical measurements[9,18,19] and colorimetric sensing.[20]

An important component of an oxygen sensor is the matrix in which the emitting dyes are immobilized. The matrix materials impact the sensing ability mainly in two ways: first by the permeability to oxygen, which allows for fast diffusion of oxygen to the emitting molecules for quenching; second by

Received: February 21, 2012
Revised: May 24, 2012
Published: May 24, 2012

Scheme 1. Synthetic Path for Blue Emitting Dyes[a]

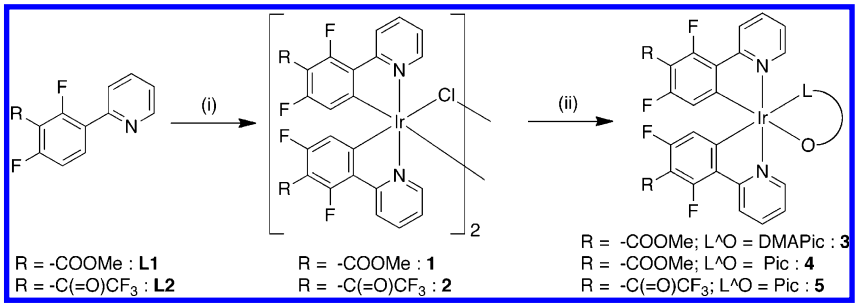

[a](i) **L1:** $IrCl_3$, x·H_2O, 2-ethoxyethanol/H_2O, 125 °C, 18 h; **L2**: $IrCl_3$, x·H_2O, 2-ethoxyethanol, 125 °C, 18 h; (ii) DMAPic = 4-N,N-dimethylaminopicolinic acid or Pic = picolinic acid, TBAOH, CH_2Cl_2, 40 °C, 12 h.

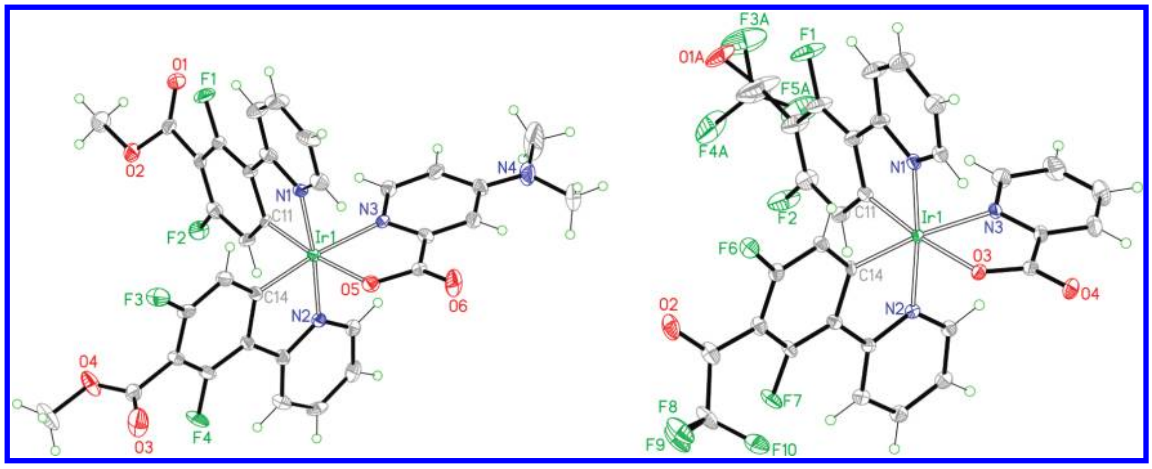

Figure 1. Ortep drawings of **3** (left) and **5** (right).

their chemical nature leading to different aggregation of the dyes resulting in different accessibility of the dyes by oxygen. The aluminum oxide-hydroxide nanostructured solid support AP200/19 has recently shown very good performances for oxygen sensing using charged bis-cyclometalated iridium(III) complexes.[16,17] Herein we report on the use of neutral blue phosphorescent iridium(III) complexes immobilized in AP200/19. In addition to providing oxygen sensing in the blue region of the visible spectrum, it is the first evaluation of neutral dyes with the AP200/19 matrix.

First, we briefly describe the synthesis, characterization, and theoretical calculation rationalizing the properties of the new dyes. To obtain emission in the blue region, we developed new phosphorescent emitters using ester and trifluoromethyl ketone groups. The trifluoromethyl ketone was expected to lead to deeper blue and high solubility, while the ester would be an interesting group for future grafting of the dyes onto specific substrates through carboxylic acid attachment to an inorganic material. Second, we evaluated the oxygen sensing properties of the dyes by their physical immobilization in a matrix. For this evaluation, two types of matrices were selected: a classical polystyrene membrane and the novel aluminum oxide-hydroxide nanostructured matrix, AP200/19. Polystyrene films show different compatibility with dyes depending on their polarity, and they provide good permeability to oxygen while preventing other quenchers to interact with the dye.[13] The metal oxide matrix is expected to provide a better sensitivity by driving the oxygen into the nanopores and isolating the dyes from each other.[15] The influence of plasticizer on the sensing ability of the polymeric film was analyzed and compared to the positively charged nanostructure which has been never used in combination with noncharged complexes.

RESULTS AND DISCUSSION

Synthesis and Characterization. Scheme 1 represents the route for the synthesis of the blue emitting dyes. The preparation of the ligands started with 2-(2,4-difluorophenyl)-pyridine. The proton between the two fluorine atoms is significantly acidic due to the strong acceptor character of the neighboring halogens. Therefore deprotonation by *n*-butyl lithium (n-BuLi) or lithium diisopropyl amine (LDA) followed by quenching of the intermediate anion with the required electrophile leads to the desired substitution. Ligand **L1** is obtained quenching with CO_2 followed by esterification with methanol. In the case of ligand **L2** quenching by ethyl trifluoroacetic acid leads to a mixture of ligand **L2** and its reduced form, 2-(2,4-difluoro-3-(2,2,2-trifluoroethanol)-phenyl)pyridine (**L2b**). The two products **L2** and **L2b** can be separated by silica gel column chromatography. **L2b** can be oxidized to **L2** using a procedure based on copper chloride (see details for the ligands in the SI). The chloro-bridged iridium dimer **1** has been synthesized following the classical procedure based on iridium tris-chloride heated in a mixture 2-ethoxyethanol/water in the presence of a slight excess of the ester substituted ligand **L1**. On the other hand, we found that in those conditions **L2** leads to mixtures of complexes with the trifluoromethyl ketone group reduced to the alcohol and/or hydrated. We could isolate the pure iridium dimer by performing the reaction in pure 2-ethoxyethanol. To synthesize the final dyes it was necessary to avoid saponification for **3** and

dx.doi.org/10.1021/cm300575z | *Chem. Mater.* 2012, 24, 2330−2338

Table 1. Photophysical and Electrochemical Data of the Dyes in Acetonitrile[g]

	absorption[a]	emission in solution[b]					redox[c]		DFT/M06	
	λ_{abs} (nm) (ε, 10^3 L mol^{-1} cm^{-1})	λ_{max} (nm)	Φ_{em}	τ (μs)	k_r[d] (10^5 s^{-1})	k_{nr}[d] (10^5 s^{-1})	E_{ox} (V)	E_{red} (V)	IE[e](eV)	EA[f](eV)
3	248 (44.7), 284 (49.9) 380 (4.9), 452 (0.5)	470	0.39	1.78	2.19	3.43	1.04	−2.36	5.90	−2.18
4	252 (46.3),282 (33.2), 372 (4.8), 450 (0.3)	463	0.44	1.94	2.27	2.89	1.07	−2.28	5.99	−2.23
5	255 (44.9), 291 (31.1) 346 (18.1), 445 (0.5)	459	0.08	2.29	0.35	4.02	1.22	−1.85 −2.36	6.21	−2.59

[a]Acetonitrile at room temperature. [b]Degassed acetonitrile at room temperature. [c]0.1 M $TBAPF_6$, in acetonitrile, potentials vs ferrocenium/ferrocene. [d]Calculated using the relations $k_r = \Phi_{em}/\tau$ and $k_{nr} = 1/\tau - k_r$. [e]Theoretical vertical ionization energies computed at the DFT/M06 level of theory. [f]Theoretical vertical electron affinity energies computed at the DFT/M06 level of theory. [g]τ: lifetime of excited state; Φ_{em}: photoluminescence quantum yield in solution.

4 and hydrolysis in the case of **5**. Therefore the ancillary ligand (DMAPic or Pic) was refluxed with a default of tetrabutyl ammonium hydroxide (TBAOH) prior to the addition of the chloro-bridged dimer. Following this procedure the reactions proceed smoothly, and the blue emitting dyes are obtained with good yields, >70%.

Single crystals of **3** and **5** suitable for X-ray diffraction analysis have been grown by slow diffusion of hexane into a dichloromethane solution of the complexes. ORTEP drawings of the structures are shown in Figure 1, and selected crystallographic data are provided in Table S1 and Table S2. The two complexes have the expected octahedral coordination geometry around the iridium center with the cis-C,C trans-N,N chelate configuration. It should be noted that the ester and trifluoroethanone groups are out of the plane of the cyclometalated ligands, while the *N,N*-dimethyl-amino group of **3** is in the same plane as the pyridine of the ancillary ligand.

Electrochemistry. Electrochemical potentials are reported vs ferrocenium/ferrocene in Table 1. The complexes **3**, **4**, and **5** show reversible oxidation processes at 1.04, 1.07, and 1.22 V vs Fc^+/Fc, respectively. The higher oxidation potential for **5** compared to **4** reflects the significantly stronger acceptor character of the trifluoroethanone than the methyl ester group (Hammett parameters: $COCF_3$: σm = 0.63, σp = 0.80; COOMe: σm = 0.37, σp = 0.45).[21] Results from theoretical calculations present the same trend for the vertical ionization potentials (IE) of the three compounds. A difference of 0.09 eV is found between the computed IEs of **3** and **4**. Complex **5** exhibits a higher IE, lying at 0.31 and 0.22 eV from **3** and **4**, respectively.

Based on both σm and σp Hammett parameters, the reduction potentials are in the range expected[22] but for **5** which is much lower than anticipated (−1.85 V vs Fc^+/Fc). By analogy with the reduction potential of α,α,α-trifluoroacetophenones (−1.42 vs SCE[23] in acetonitrile that is ≈−1.8 vs Fc^+/Fc) we attribute the first reduction of **5** to the reduction of the trifluoroethanone group instead of the cyclometalated ligand as usually found in such complexes. This finding correlates well with the LUMO localization of **5**, which is found to be mostly on the $-COCF_3$ moieties (Figure 3), in contrast with the other two compounds. As a result, the electron affinity (EA) of **5** is computed to be 0.36 eV (0.41 eV) lower than the one of **4** (**3**), which reflects the same trend than the experimental values for E_{red}.

Photophysical Properties. UV−visible absorption spectra have been measured in acetonitrile solution at room temperature (Figure 2 and Table 1). They display strong bands in the UV up to 300 nm attributed to intraligand ($\pi-\pi^*$) transitions.

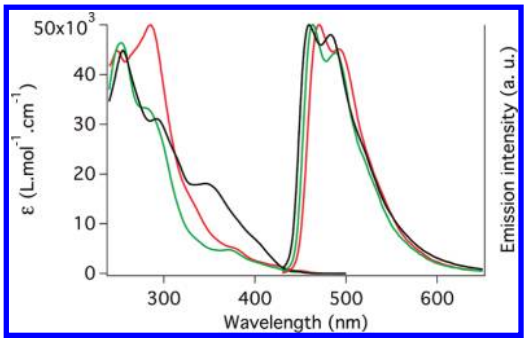

Figure 2. Absorption (left) and emission (right) spectra in acetonitrile at room-temperature of **3** (red), **4** (green), and **5** (black).

Lower-energy absorption bands correspond to metal-to-ligand charge transfer (MLCT) transitions. Finally, weak bands with $\varepsilon \sim 400$ M^{-1} cm^{-1} are ascribed to spin-forbidden transitions directly to triplet states. Overall, the three spectra have similar band positions however significant differences in absorption coefficient are observed. A first band around 250 nm is similar for the three complexes with absorption coefficient about 45,000 M^{-1} cm^{-1}. The second band around 385 nm has similar intensity (about 32,000 M^{-1} cm^{-1}) for **4** and **5**, while **3** is stronger (50,000 M^{-1} cm^{-1}); it is therefore attributed to a $\pi-\pi^*$ transition involving the ancillary ligand. MLCT transitions from about 350 nm for all complexes are similar for **3** and **4** (about 5,000 M^{-1} cm^{-1}) while **5** has significantly more intense transitions (18,000 M^{-1} cm^{-1} at 348 nm and 7,000 M^{-1} cm^{-1} at 400 nm). This points to a higher MLCT character for **5**. LR-TDDFT calculations confirm that the first singlet vertical excitation of **5** possesses the largest oscillator strength among the three complexes, due to the enhanced delocalization of the excited electron over the $-COCF_3$ moieties and the ppy ligands (**3**: 390 nm, oscillator strength = 0.0363; **4**: 385 nm, oscillator strength = 0.0430; **5**: 385 nm, oscillator strength = 0.1365).

When **3**, **4**, and **5** in solution in acetonitrile are excited in the MLCT bands, they show sky-blue emission with photoluminescence quantum yield Φ_{em} of 0.39, 0.44, and 0.08, respectively (Figure 2 and Table 1). As expected from the presence of additional strong acceptor groups on the cyclometalated phenyl, the emission maxima are blue-shifted for the three complexes when compared to the classical sky-blue emitter FIrPic (λ_{max} = 470 nm in acetonitrile), [Ir(2-(2,4-difluorophenyl)pyridine)$_2$(picolinate)]. The ester group results in a 7 nm blue shift similar to our previous report with charged complexes based on carbene ancillary ligands,[24] and the

dx.doi.org/10.1021/cm300575z | *Chem. Mater.* 2012, 24, 2330−2338

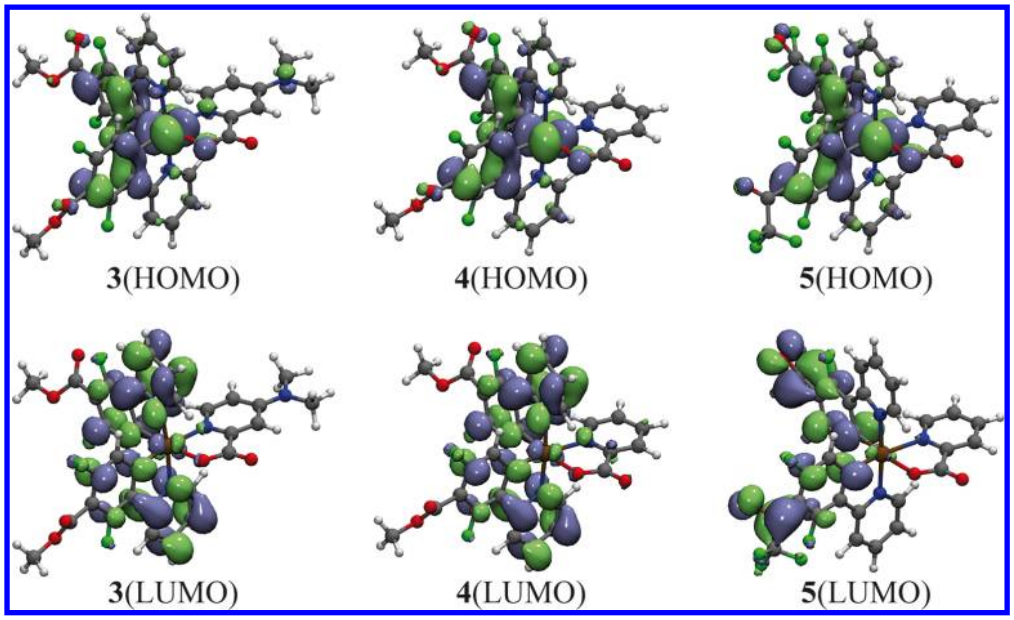

Figure 3. Kohn–Sham HOMO and LUMO for compounds **3**, **4**, and **5** computed for the ground state geometry at the DFT/M06 level of theory. Isosurfaces are set to 0.03 au.

trifluorethanone group further blue shifts the emission to 459 nm. The donor effect of DMAPic is seen as red shifting the emission compared to nonsubstituted pic.[25]

For complexes **3**, **4**, and **5** the excited state lifetimes are 1.78, 1.94, and 2.29 μs, respectively. Assuming unitary intersystem crossing quantum yield, radiative (k_r) and nonradiative (k_{nr}) decay rates can be calculated from phosphorescence quantum yields and lifetimes. This leads to a radiative lifetime τ_{rad} (respectively k_r) of 4.56 μs (2.19×10^5 s^{-1}), 4.40 μs (2.27×10^5 s^{-1}), and 28.6 μs (0.35×10^5 s^{-1}) for **3**, **4**, and **5**, respectively. **3** and **4** are very similar as the nonchromophoric ancillary ligands are closely related.[26] On the other hand, **5** has very different radiative properties, attributed to the lower lying LUMO introduced by the $COCF_3$ group, as supported by theoretical calculations.

ΔSCF calculations on T_1 of **3** and **4** provide energy differences between the first triplet state and the ground state in agreement with the measured emission, 2.63 eV (exp.: 2.64 eV) and 2.63 eV (exp.: 2.68 eV), respectively. The character of T_1 can in both cases be defined as a MLCT-LC (see spin density plot in Figure 4). For **5**, the direct optimization of T_1 provides an electronic state where the excited electron occupies a π^* orbital mostly localized on the $-COCF_3$ group, as expected from the calculated LUMO for the ground state (Figure 3). This triplet state lies at 2.22 eV above the ground state (see spin density plot in Figures 4 and 5(a)). Another triplet state can be formed by populating the first unoccupied π^* orbital located on the ppy ligand. After geometry optimization of this state, the transition energy (2.65 eV) obtained from ΔSCF matches well the experiment value 2.70 eV. This triplet state is similar to the first one of compounds **3** and **4** and therefore possesses the expected MLCT-LC character (see spin density plot in Figures 4and 5(b)). Even though a complete discussion of the nonradiative paths and radiative properties of **5** is outside the scope of this article and would necessitate the inclusion of spin–orbit coupling, the presence of low-lying triplet states could help in explaining the weaker quantum yield and the long radiative lifetime of **5**.

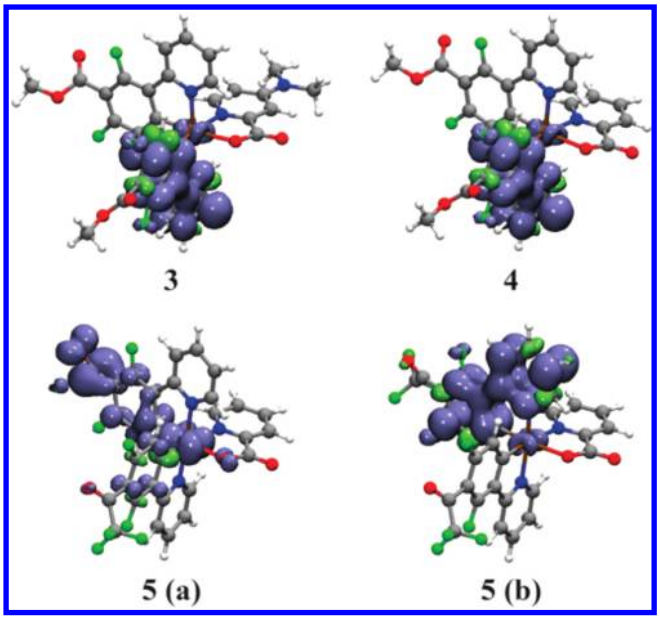

Figure 4. Spin density for each computed compound resulting from the unrestricted DFT calculations of triplet states (isovalue set to 0.003 au).

Oxygen Sensing. To evaluate the oxygen sensing properties of the dyes, both a nanostructured metal oxide matrix, AP200/19, and a polymeric polystyrene membrane were used to physically immobilize the dyes. Table 2 shows the composition and the nomenclature of the different polystyrene (PS) cocktails, with and without the plasticizer *o*-cyanophenyl octyl ether (*o*-CPOE) as well as the one for the nanostructured matrix.

Table 3 shows the luminescence excitation and emission properties of the different sensing layers. As can be seen compared to Table 1, where the spectrum is recorded in solution, the incorporation of the dyes into a solid support slightly changes the emission properties of the dyes, which is attributed to the change of environment.

dx.doi.org/10.1021/cm300575z | *Chem. Mater.* 2012, 24, 2330–2338

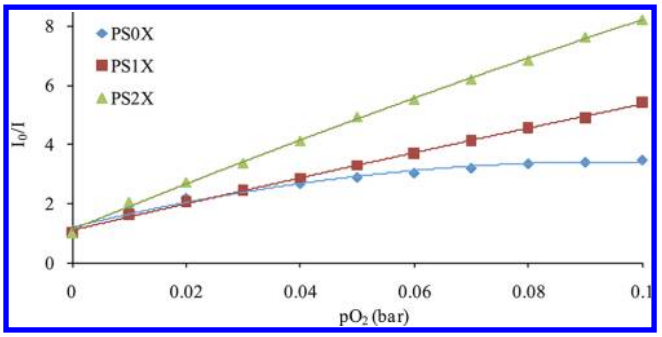

Figure 5. Stern–Volmer plot obtained for plasticizer free (PS0X) and nonfree (8.5 wt % for PS1X and 17.5 wt % for PS2X) polymeric membranes of dye **3**. Dye concentration = 1.5 mg mL^{-1}; $\lambda_{exc/em}$ = 303/470 nm; slit width$_{exc/em}$ = 20/20 nm, t_d = 120 μs, and t_g = 5 ms.

Table 2. Nomenclature and Composition of the Oxygen-Sensitive Membranes[a]

name	wt % PS	wt % *o*-CPOE	wt % dye
PS0X	98.5	0	1.5
PS1X	90	8.5	1.5
PS2X	81	17.5	1.5
AP200/19	-	-	1.5

[a]PS, polystyrene; *o*-CPOE, *o*-cyanophenyl octyl ether; AP200/19, aluminum oxide hydroxide nanostructured matrix.

Table 3. Maxima Luminescence Excitation and Emission Wavelengths, $\lambda_{exc/em}$, for the Dyes Incorporated into Polystyrene (PS) and Metal Oxide Matrix AP200/19[a]

membrane	**3** $\lambda_{ex/em}$ (nm)	**4** $\lambda_{ex/em}$ (nm)	**5** $\lambda_{ex/em}$ (nm)
PS0X	303/470	300/470	300/465
PS1X	303/470	300/470	300/465
PS2X	303/470	300/470	300/465
AP200/19	335/470	335/467	340/465

[a][dye] = 1.5 mg mL^{-1}; monochromator slit width$_{exc/em}$ = 20/20 nm.

For all the membranes, similar emission profiles were obtained, and the luminescence was completely quenched when molecular oxygen concentration is over 10% (see the SI). Since in all the cases the lifetime was lower than 50 μs, it was not possible to measure the luminescence lifetime with our available instrumentation, which does not provide reliable data with lifetimes below 50 μs. Therefore, the oxygen sensing properties were evaluated by the reduction in emission intensity when different quencher (oxygen) concentrations are present. This reduction in intensity is described by the Stern–Volmer equation (see eq 1)

$$\frac{I_0}{I} = 1 + k_{SV}pO_2 \quad (1)$$

where I is the luminescence intensity, the subscript "0" refers to the value in the absence of quencher, k_{SV} is the Stern–Volmer constants, and pO_2 is the partial pressure of oxygen.

The heterogeneity of the medium where the dyes are immobilized often causes a deviation in the linearity of the response in the Stern–Volmer equation. The downward deviation is usually explained by the presence of sites within the matrix with different accessibility to oxygen. Consequently, the dyes are quenched differently depending on their accessibility by oxygen, which results in different Stern–Volmer constants for each site.[15–17] In this case, a multisite model, each having a linear behavior, is necessary to describe the response of the films to the presence of oxygen. Generally, the two-site model proposed by Demas and co-workers, so-called Demas' model,[27] is applied (see eq 2)

$$\frac{I_0}{I} = \left[\frac{f_1}{1 + k_{SV1}pO_2} + \frac{f_2}{1 + k_{SV2}pO_2}\right]^{-1} \quad (2)$$

where f_i denotes the fractional contribution of the total luminescence emission from the luminophore located at site type i under unquenched conditions, which exhibit a discrete Stern–Volmer quenching constant given by k_{SVi}.

Table 4. Oxygen Sensitivity, $\Delta I_{1\%}$ and $pO_2(S = 1/2)$, of the Dyes Incorporated into PS Films and the AP200/19 Nanostructure[a]

		Demas' model					Lehrer's model				
		k_{SV1} (bar^{-1})	f_1	k_{SV2} (bar^{-1})	f_2	r^c	k_{SV} (bar^{-1})	f_0	r^c	$\Delta I_{1\%}$ (%)[a,d]	$pO_2(S = 1/2)$ (mbar)[a,e]
3	PS0X	134.65 ± 27.53	0.71 ± 0.02	2.02 ± 0.27	0.28 ± 0.02	0.9999	106.47 ± 13.17	0.78 ± 0.01	0.9984	43.49	16.77
	PS1X	42.48 ± 0.51[b]	1.00 ± 0.00	-	-	0.9992	42.48 ± 0.51[b]	1.00 ± 0.00	0.9992	36.70	23.54
	PS2X	198.60 ± 62.67	0.67 ± 0.07	21.10 ± 4.10	0.33 ± 0.08	0.9998	89.82 ± 0.26	0.96 ± 0.00	0.9988	51.40	12.22
	AP 200/19	780.77 ± 18.28	0.91 ± 0.00	8.68 ± 1.05	0.05 ± 0.01	0.9913	568.62 ± 49.44	0.98 ± 0.01	0.9901	86.47	1.83
4	PS0X	150.30 ± 63.30	0.64 ± 0.09	2.14 ± 0.1	0.35 ± 0.10	0.9849	106.25 ± 28.60	0.72 ± 0.1	0.9938	39.79	21.57
	PS1X	48.56 ± 1.84[b]	1.00 ± 0.00	-	-	0.9989	48.56 ± 1.84[b]	1.00 ± 0.00	0.9989	40.18	20.60
	PS2X	168.23 ± 21.61	0.71 ± 0.06	17.21 ± 0.07	0.28 ± 0.07	0.9999	89.55 ± 4.72	0.95 ± 0.01	0.9989	51.15	12.41
	AP 200/19	667.06 ± 185.41	0.89 ± 0.01	11.84 ± 0.01	0.08 ± 0.01	0.9937	392.98 ± 63.47	0.97 ± 0.00	0.9913	81.58	2.70
5	PS0X	178.41 ± 8.55	0.74 ± 0.03	3.38 ± 1.13	0.25 ± 0.03	0.9869	125.40 ± 9.77	0.83 ± 0.04	0.9855	50.83	12.17
	PS1X	57.30 ± 2.54[b]	1.00 ± 0.00	-	-	0.9996	57.30 ± 2.54[b]	1.00 ± 0.00	0.9996	44.06	17.46
	PS2X	355.40 ± 8.55	0.50 ± 0.02	32.56 ± 1.14	0.50 ± 0.02	0.9988	83.44 ± 1.07	0.97 ± 0.01	0.9978	49.65	12.82
	AP 200/19	748.66 ± 56.84	0.90 ± 0.02	16.04 ± 7.73	0.06 ± 0.01	0.9974	485.25 ± 15.03	0.99 ± 0.00	0.9962	85.11	2.12

[a][dye] = 1.5 mg mL^{-1}; slit width$_{exc/em}$ = 20/20 nm; t_d = 120 μs; t_g = 5 ms; for $\lambda_{exc/em}$ see Table 3, the experimental results have been expressed as the average of 3 replicas ± $s{\cdot}t/\sqrt{n}$ (n = 3, t = 4.30 ($2P$ = 0.05)). [b]Values obtained by a linear fitting. [c]Regression coefficient of the model fit. [d]$\Delta I_{1\%}$ is the percentage of quenching reached when the oxygen concentration in the media is 1% (v/v), compared with the total available quenching. [e]$pO_2(S = 1/2)$ is the partial pressure of oxygen necessary to reduce 50% of the initial (oxygen free) luminescence exhibited by the film.

dx.doi.org/10.1021/cm300575z | *Chem. Mater.* 2012, 24, 2330–2338

Another two-site model was proposed by Lehrer.[28] In this model, only one microenvironment is accessible to the quencher (therefore $k_{SV2} = 0$; see eq 3)

$$\frac{I_0}{I} = \left[\frac{f_0}{1 + k_{SV}pO_2} + (1 - f_0)\right]^{-1} \quad (3)$$

where f_0 denotes the fraction of the total luminophore's population that the quencher is able to access, and k_{SV} is the Stern−Volmer quenching constant associated with the accessible fraction of luminophores.

Table 4 shows the Stern−Volmer constants for each film according to Demas' and Lehrer's Models. In most cases the dye is located in two different environments, except for the polymeric sensing films containing 8.5 wt % of plasticizer (named PS1X), where the quenching follows linearly the standard Stern−Volmer equation. In all other cases the relationship between oxygen concentration and I_0/I does not follow a linear relationship (see the SI), and Demas' and Lehrer's models were used to adjust the experimental data. Similar results have been found using similar dyes and supports.[14−17]

The fact that the nonlinear results can be adjusted using both models may be explained by looking at the results for the membranes PS0X reported in Table 4. For Demas' model, k_{SV1} is much higher than k_{SV2}, and the fractional contribution of the sites possessing k_{SV2} (expressed with f_2) is lower than the contribution of the sites having k_{SV1}. Therefore, the sensitivity to oxygen associated with the second group of sites can be neglected, which leads to Lehrer's model, where only one of the sites is quenched by oxygen. However, by using Lehrer fitting, the quenching capacity associated with this second site is not taken into account, which produces a decrease in the k_{SV} of PS2X compared to PS0X for the Lehrer model, when it possesses, in fact, a better sensitivity (Table 4 and Figure 5).

The results found in the polymeric films when comparing both models can be explained by the heterogeneity of the media and the aggregation of the dye, which are frequent on polymeric films.[14,16,17] The addition of the right amount of plasticizer appears important to control the homogeneity of the media, leading to a linear response to oxygen, always an advantage in terms of calibration for further implementation as oxygen sensors. As can be seen in Figure 5 for the polymeric membranes of the dye **3**, the presence of plasticizer increases the sensitivity to oxygen of the film in the site possessing k_{SV2} (in the high O_2 concentration of the range studied), whose value goes from 2.02 bar^{-1} for the plasticizer-free membrane (PS0X) to 21.10 bar^{-1} for PS2X, improving the sensing capability of the membrane. Similar behaviors were found for dyes **4** and **5**.

Generally, plasticizers improve the mechanical properties of the matrix, the solubility of the components in the membrane, and increase the diffusion of oxygen.[29−31] These aspects may be responsible for the linearity and improvement in oxygen sensitivity of PS1X and PS2X. Although an increase in the viscosity often decreases the sensitivity of the membranes, the compatibility between the plasticizer and the polymer seems to be the most important factor which determines the sensitivity of the membranes.[29,30] In addition, the use of plasticizer improves the efficiency of the luminescence. Indeed, the voltage of the photomultiplier was decreased while keeping the level of the emission peak, when increasing the amount of plasticizer (see the SI), in contrast to previous reports using charged iridium complexes where plasticizers can act as a quencher of the luminescence.[16,17] Here, the improved solubility of the dye and permeability to oxygen of the film seems to thwart these issues, resulting in an enhancement of the sensitivity for the membranes containing high plasticizer concentration, as can be noticed in Figure 5 and confirmed with the data showed in Table 4 for Demas' model.

The incorporation of the dyes into AP200/19 provides higher k_{SV} than the immobilization into the PS-matrix. For all dyes, the sensitivity to oxygen (concentration between 0 and 10% in volume) of the metal oxide hydroxide nanocomposite is about 4 times higher than with the polymeric matrix. The metal oxide matrix is formed from agglomerated nanoparticles, where the nanopores are located inside while the macropores appear between agglomerated particles.[32] Therefore, the heterogeneity of the nanostructured oxide hydroxide membranes is responsible for the nonlinearity response to oxygen, in which one of the sites is highly sensitive to oxygen, as previously demonstrated by Fernandez-Sanchez et al.[32] The capillary forces are responsible for this high sensitivity since they drive the oxygen quickly into the nanopores,[14] in line with previous reports using this nanostructure in combination with charged Ru(II) and Ir(III) dyes.[14,16,17] The AP200/19 matrix is positively charged, and its compatibility with charged complexes has proved to improve the sensitivity to oxygen in different degree depending on the properties of the dyes.[14,16,17] However, this is the first time that this metal oxide nanostructure is used in combination with noncharged complexes. The results confirm and generalize its suitability to enhance the oxygen sensing ability for low oxygen concentration.

Overall, dye **3** supported in the oxide hydroxide nanostructure is the most sensitive film according to both Lehrer and Demas' models from 0 to 10% O_2 (k_{SV1} = 780.77 ± 18.28 bar^{-1}). Nevertheless, dye **5** immobilized into the nanostructured matrix possess a similar sensitivity to oxygen (k_{SV1} = 748.66 ± 56.84 bar^{-1}). Furthermore, for classic polymeric membranes, dye **5** provides a better sensitivity to oxygen than **3** and **4**. This behavior is attributed to the higher radiative lifetime of dye **5**, which usually provides a better sensitivity to oxygen.

Figure 6 gives an example of the high sensitivity to low oxygen concentration. Already for 1% of oxygen, the intensity of luminescence is practically totally quenched. This intensity drop can be compared with the parameters $\Delta I_{1\%}$ and $pO_2(S = 1/2)$ as rough guides of the sensitivity of the optical oxygen sensing films to low oxygen concentrations (Table 4).[16] $pO_2(S$

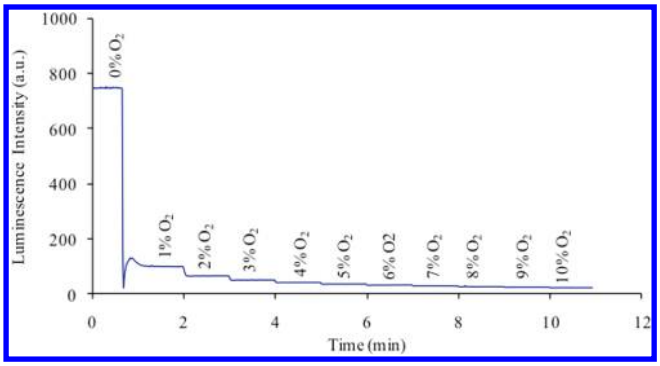

Figure 6. Example of time trace curve for the AP200/19 membrane of dye **3**. Dye concentration = 1.5 mg mL^{-1}; $\lambda_{exc/em}$ = 335/470 nm; slit $width_{exc/em}$ = 20/20 nm, t_d = 120 μs, and t_g = 5 ms.

dx.doi.org/10.1021/cm300575z | Chem. Mater. 2012, 24, 2330−2338

= 1/2) is defined as the partial pressure of oxygen necessary to reduce 50% of the initial (oxygen free) luminescence exhibited by the film. Similarly, $\Delta I_{1\%}$ is defined as the percentage of quenching reached when the oxygen concentration in the media is 1% (v/v), compared with the total available quenching. The practical pressure necessary to quench the luminescence by 50% is higher for the polymeric films than for the metal oxide hydroxide matrix, whose intensity is quenched by 50% with less than 0.003 bar. Furthermore, when the oxygen concentration is 1%, the nanostructure leads to more than 80% of luminescence quenching, while only 50% is reached with the polymeric films. This clearly shows the high potential of this metal oxides hydroxide nanostructure to serve as matrices for oxygen trace sensors.

■ CONCLUSION

Three new neutral blue emitting cyclometalated iridium(III) complexes have been synthesized and characterized by means of spectroscopic and electrochemical methods and X-ray crystal structure. In addition to fluorine, the dyes use methyl ester (−COOMe) and trifluoroethanone ($-COCF_3$) groups as strong acceptor to blue shift the emission compare to FIrPic. Interestingly the $-COCF_3$ group changes the LUMO localization, which is found to be mostly on the $-COCF_3$ moieties, in contrast to usual complexes based on 2-phenylpyridine skeleton.

All three dyes were investigated in order to evaluate their potential as oxygen-sensitive chemical sensors in the blue region of the visible spectrum. The dyes were physically immobilized into a nanostructured metal oxide matrix, AP200/19, and a classical polymeric polystyrene membrane, showing in both cases a single emission band, which is totally quenched for oxygen concentrations over 10%.

The sensitivity to oxygen was evaluated according to Demas and Lehrer's models and shows that the oxygen sensing properties are the result of interplay between the performance and aggregation of the dye and the film morphology. The use of different amounts of plasticizer has an impact on the aggregation behavior of the dyes and oxygen diffusion, overall improving the oxygen sensing ability.

On the other hand, the most sensitive films are based on the AP200/19, which shows in all cases a Stern−Volmer constant 4 times higher than the polystyrene classic membrane. In addition $pO_2(S = 1/2)$ and the parameter $\Delta I_{1\%}$ were evaluated in order to establish the ability of the membranes to be sensitive to low oxygen concentrations. In all the cases the metal oxide hydroxide nanostructure provides the best results, probably due first to the more rigid environment and more homogeneous distribution of the dye in the mesoporous structure, avoiding the energy transfer between the molecules, and second to the nanostructure of the matrix improving oxygen diffusion. These results confirm the suitability of this type of nanostructure to improve the oxygen sensitive properties of noncharged complexes. Nevertheless, further studies about the stability, the dye migration, and the sensitivity below 1% oxygen will be necessary for the implementation as oxygen trace sensors in intelligent food packages[33] or chambers with electrical equipment where oxygen leakages can be harmful.[34]

■ EXPERIMENTAL SECTION

Materials and Methods. Iridium trichloride hydrate was purchased from Heraeus. Tetrabutyl ammonium hydroxide (TBAOH) was used as the hydrate (30 water molecules per TBAOH molecule). 2,6-Difluoro-3-(pyridine-2-yl)benzoic acid was prepared as reported in the literature.[35] All materials and solvents were of reagent quality and used as received. ^1H and ^{13}C NMR spectra were recorded using a Bruker AV 400 MHz spectrometer. Chemical shifts δ (in ppm) are referenced to residual solvent peaks. For ^1H NMR: $CDCl_3$, 7.24 ppm; for ^{13}C NMR: $CDCl_3$, 77.0 ppm. High-resolution mass spectra (HRMS) were obtained with a Waters Q-TOF-MS instrument using electrospray ionization (see the SI). UV−visible spectra were recorded in a 1 cm path length quartz cell on a Cary 100 spectrophotometer. Emission spectra were recorded on a Fluorolog 3−22 using a 90° optical geometry. The photoluminescence quantum yields were determined using fluorescein (10^{-5} M in 0.1 M NaOH; air equilibrated; QY = 0.93) as standard.[36] Excited-state lifetimes were measured using a FL-1061PC TCSPC and 406 nm Nanoled as excitation source. Voltammetric measurements employed a PC controlled AutoLab PSTAT10 electrochemical workstation and were carried out in an Ar-filled glovebox, oxygen and water <1 ppm. Cyclic Voltammetry (CV) and Differential Pulse Voltammetry (DPV) techniques were used to estimate the redox potentials. DPV was used in support to the CV to have a better estimate of the electrochemical potentials when the systems show behavior next to the irreversibility, i.e. one of the two peaks in the CV is not well-defined. DPVs were carried out sweeping from negative to positive potentials and mean values are calculated. CVs were obtained at a scan rate of 1 and 0.1 $V{\cdot}s^{-1}$. DPVs were obtained at a modulation potential of 50 mV, a step potential of 10 mV, a modulation time of 50 ms, and an interval time of 100 ms. Measurements were carried out using 0.1 M $TBAPF_6$ as supporting electrolyte in acetonitrile (MeCN). Glassy carbon, platinum plate, and platinum wire were used as working, counterm and quasi-reference electrodes, respectively. At the end of each measurement, ferrocene was added as internal reference. Data collections for X-ray crystal structures were performed at low temperature [100(2) K] using Mo K_α radiation on a Bruker APEX II CCD diffractometer equipped with a kappa geometry goniometer. All data sets were reduced by EvalCCD[37] and then corrected for absorption.[38] The solutions and refinements were performed by SHELX.[39] The crystal structures were refined using full-matrix least-squares based on F^2 with all non-hydrogen atoms anisotropically defined. Hydrogen atoms were placed in calculated positions by means of the "riding" model. In both structures disordered solvent molecules (CH_2Cl_2) were treated by SQUEEZE,[40] and additional twinning problems were carefully analyzed by TWINROTMAT[40] (in the case of **3** a new data set was created and then used for refinement, obtaining 4 BASF parameters: 0.0107(13), 0.0040(7), 0.0054(7), 0.0045(8); in the case of **5** a TWIN matrix [1 0 0 0 −1 0 0 0 −1] was directly applied to the original data set with a final BASF parameter of 0.0040(2)). Disorder problems dealing with one $-COCF_3$ moiety were found during the last stages of refinement of **5** and treated by the split model combined with some restraints (SIMU card).

Tetrakis-(L1)-μ-(dichloro)-diiridium(III) (1). A mixture of $IrCl_3$, $x{\cdot}H_2O$ with 2.3 eqiv of **L1** in a 3:1 mixture of 2-methoxyethanol and water was heated to 125 °C for 18 h. After having been cooled, the complex was precipitated with H_2O. The precipitate was isolated by vacuum filtration through a fritted glass and washed copiously with water and hexanes. The yellow solid was vacuum-dried to yield **1** (average yield about 80% on gram-scale). ^1H NMR ($CDCl_3$, 400 MHz): 9.07 (d, 4H, J = 5.6 Hz); 8.37 (d, 4H, J = 8.8 Hz); 7.89 (t, 4H, J = 7.2 Hz); 6.89 (t, 4H, J = 7.2 Hz); 5.29 (d, 4H, J = 10.4 Hz); 3.83 (s, 12 H).

Tetrakis-(L2)-μ-(dichloro)-diiridium(III) (2). $IrCl_3{\cdot}nH_2O$ (1.72 g, 4.88 mmol) was dissolved in 2-ethoxyethanol (150 mL) and degassed with argon at 75 °C for 30 min. Then 2.2 equiv of **L2** (3.11 g, 10.8 mmol) was added directly, and about 10 mL of 2-ethoxyethanol was used for rinsing. The mixture was heated to 125 °C for 18 h under argon and protected from light with an aluminum foil. After having been cooled to about 50 °C, solvent was reduced to half volume under vacuum. After having been cooled to room temperature, the mixture was poured into an Erlenmeyer flask containing 600 mL of deionized water, and an additional 100 mL of deionized water was used for

rinsing the reaction flask. Those steps were performed in air and without full protection from light. The flask was stored in the fridge (about 6 °C) for 4 h. The precipitate was isolated by vacuum filtration through a fritted glass and washed copiously with water. The yellow solid was vacuum-dried at room temperature overnight, protected from light with an aluminum foil, to yield **2** as a yellow solid (3.59 g, 2.24 mmol, yield = 92%). ^{1}H NMR ($CDCl_3$, 400 MHz): 9.07 (dd, 4H, J = 6.4, 0.8 Hz); 8.42 (d, 4H, J = 8.4 Hz); 7.99 (t, 4H, J = 9.2 Hz); 6.89 (t, 4H, J = 9.2 Hz); 5.42 (d, 4H, J = 10.4 Hz).

[Ir(L1)$_2$(4-(*N*,*N*-dimethylamino)picolinate)] (3). A mixture of 4-dimethylamino-picolinic acid (91 mg, 4 equiv) and TBAOH (330 mg, 3 equiv) in dichloromethane was refluxed at 40 °C for half an hour and cooled down to 30 °C. **1** (198 mg, 1 equiv) was added to the TBA 4-DMA-picolinate mixture. The mixture was heated at 40 °C for 12 h under argon protected from light with an aluminum foil. The mixture was cooled to room temperature and deposited on top of a silica column (SiO_2/CH_2Cl_2). The product was eluted using CH_2Cl_2/MeOH 0 to 5% to yield **3** as a yellow powder (177 mg, 76%). ^{1}H NMR ($CDCl_3$, 400 MHz): 8.77 (dd, 1H, J = 5.2, 1.2 Hz); 8.33 (d, 1H, J = 8.8 Hz); 8.26 (d, 1H, J = 8.4 Hz); 7.81 (m, 2H); 7.60 (dd, 1H, J = 5.6, 1.6 Hz); 7.52 (d, 1H, J = 3.2 Hz); 7.23 (t, 1H, J = 7.6, 1.6 Hz); 7.21 (d, 1H, J = 6.4 Hz); 7.04 (t, 1H, J = 7.6, 1.6 Hz); 6.45 (dd, 1H, J = 6.4, 3.2 Hz); 5.88 (d, 1H, J = 10.0 Hz); 5.68 (d, 1H, J = 10.0 Hz); 3.91 (s, 3H); 3.87 (s, 3H); 3.09 (s, 6H). TOF MS ES: MH$^+$ m/z: calc. 855.1420 found: 855.1389.

[Ir(L1)$_2$(picolinate)] (4). A mixture of picolinic acid (136 mg, 4 equiv) and TBAOH (665 mg, 3 equiv) in dichloromethane was refluxed at 40 °C for half an hour and cooled down to 30 °C. **1** (400 mg, 1 equiv) was added to the TBA picolinate mixture. The mixture was heated at 40 °C for 12 h under argon protected from light with an aluminum foil. The mixture was cooled to room temperature and deposited on top of a silica column (SiO_2/CH_2Cl_2). The product was eluted using CH_2Cl_2/MeOH 0 to 5% to yield **4** as a yellow powder (327 mg, 73%). ^{1}H NMR ($CDCl_3$, 400 MHz): 8.74 (ddd, 1H, J = 5.6, 1.6, 0.8 Hz); 8.37 (m, 2H); 8.30 (d, 1H, J = 8.4 Hz); 7.98 (td, 1H, J = 8.0, 1.6 Hz); 7.84 (m, 2H); 7.75 (ddd, 1H, J = 7.2, 1.6, 0.8 Hz); 7.46 (ddd, 1H, J = 7.6, 5.6, 1.6 Hz); 7.41 (ddd, 1H, J = 5.6, 1.6, 0.8 Hz); 7.27 (dt, 1H, J = 7.2, 1.6 Hz); 7.04 (dt, 1H, J = 7.2, 1.6 Hz); 5.89 (d, 1H, J = 10.0 Hz); 5.63 (d, 1H, J = 10.0 Hz); 3.92 (s, 3H); 3.88 (s, 3H). TOF MS ES: MH$^+$ m/z: calc. 812.0997 found: 812.0978.

[Ir(L2)$_2$(picolinate)] (5). A mixture of picolinic acid (500 mg, 4 equiv) and TBAOH (2.4 g, 3 equiv) in dichloromethane (100 mL) was refluxed at 40 °C for half an hour and cooled down to 30 °C. **2** (1.6 g, 1 mmol, 1 equiv) was dissolved in dichloromethane (20 mL) and added to the TBA picolinate mixture. An additional 10 mL of dichloromethane was used for rinsing. The mixture was heated at 30 °C for 12 h under argon protected from light with an aluminum foil. The mixture was cooled to room temperature and deposited on top of a silica column (SiO_2/CH_2Cl_2). The product was eluted using CH_2Cl_2/acetone 0 to 25% to yield **5** as a yellow powder (1.42 g, 80%). ^{1}H NMR ($CDCl_3$, 400 MHz): 8.78 (dd, 1H, J = 5.6, 0.4 Hz); 8.40–8.32 (m, 3H); 8.04 (td, 1H, J = 7.6, 1.2 Hz); 7.92 (m, 2H); 7.76 (ddd, 1H, J = 5.2, 1.6, 0.8 Hz); 7.53 (ddd, 1H, J = 7.6, 5.2, 1.6 Hz); 7.46 (dd, 1H, J = 5.6, 0.8 Hz); 7.35 (ddd, 1H, J = 7.6, 6.0, 1.6 Hz); 7.13 (ddd, 1H, J = 7.6, 6.0, 1.6 Hz); 6.02 (d, 1H, J = 10.0 Hz); 5.72 (d, 1H, J = 10.0 Hz). TOF MS ES: MH$^+$ m/z: calc. 888.0534 found: 888.0547.

Theoretical Calculations. Full geometry optimizations of the iridium compounds in their singlet ground state were performed with DFT using the M06 functional[41] with the relativistic effective core potential and basis set LANL2DZ[42] for the iridium, the TZVP[43,44] basis set for the remaining atoms, an ultrafine integration grid, and tight geometrical convergence criteria with the Gaussian 09 package.[45] At each ground state (singlet) geometry, LR-TDDFT calculations were performed using the same basis sets and *xc*-functional for the first 50 singlet states. Condensed-phase effects were taken into account using a self-consistent reaction-field (SCRF) model in which the solvent is implicitly represented by a dielectric continuum characterized by its relative static dielectric permittivity ε. Within the different approaches that can be followed to calculate the electrostatic potential created by the polarized continuum in the cavity, we have employed the integral equation formalism of the polarizable continuum model (IEFPCM).[46] A relative permittivity of 35.688 was employed to simulate acetonitrile,[45] the solvent used in the experimental work. To gain insights into the phosphorescence behavior of the different iridium compounds, we optimized the geometry of the first triplet state using unrestricted DFT (U-DFT) with the same basis set as described before. As suggested by a recent work,[47] we used the *xc*-functional M05-2X[48] for this task, due to its excellent performance for the emission spectra for a series of iridium-based compounds. At the minimum energy structure, we computed the difference in energy between the triplet (T_1) and singlet (S_0) state (ΔSCF method) with the inclusion of implicit solvent and obtained an estimation of the first phosphorescence band. See the Supporting Information for additional details on the calculations.

Oxygen Sensing. To obtain the polymeric films, different cocktails were prepared in sealable 4 mL flasks, filled up to 2 mL volume with chloroform (dye concentration of 1.5 mg mL^{-1}) and shaken on a Vortex-Genie 2 (Scientific Industries, Bohemia, NY, USA) equipped with a homemade holder. A nanostructure prepared by Ilford Imaging Switzerland following the procedure previously published[15−17] was also used as supporting matrix. This nanostructure is called AP200/19, and it is based on a polyethylene terephthalate (PET) thin plate coated by courting coating with aluminum oxide hydroxide, which provides a positively charged nanostructured film with a pore diameter of 19 nm and a total pore volume of 20 mL/m^2.

Once all the components were dissolved in chloroform, a Laurell spin-coater model WS-400B-6NPP/LITE (North Wales, PA, USA) was used to spin-coat the respective cocktail on the supports. For polystyrene membranes, 200 μL of the cocktail was injected onto a rotating glass plate of a spinning device at 700 rpm, while for the metal oxide nanostructured membranes, 100 μL of the cocktail was injected onto the rotating metal oxide support fixed onto a spinning device at 300 rpm. Both, PS and AP200/19 membranes were transparent and showed a thickness between 2 and 7 μm. Three replicas for each kind of membrane were prepared in order to evaluate the error. All the experimental results are expressed as the average of 3 replicas ± error ($s{\cdot}t/\sqrt{n}$), where s is the standard deviation, t is the Student's t, and n is the number of replicas.

The luminescence measurements were obtained by means of a Varian Cary-Eclipse luminescence spectrometer equipped with a Xe flash lamp (peak power equivalent to 75 kW), Czerny-Turner monochromators, R-928 photomultiplier tube which is red sensitive (even 900 nm) with manual or automatic voltage. For gas mixing, two mass flow controllers (MFC) of Type EL-FLOW model F-201CV Bronkhorst High-Tech (Ruurlo, Netherlands) were connected to copper and stainless steel tubing. These tubes connect the MFCs and a flow-through cell specially designed for the spectrometer. The system was controlled by Cary Eclipse software for Windows 95/98/NT which fully controls the luminescence spectrometer. The O_2-gas station was controlled by a self-written LabView 8.2 program connected to a Flow Bus interface (Bronkhosrt) that fully controls the Bronkhosrt mass-flow controllers via RS-232. A time trace curve was used to recorder I_0 and the intensity I at different oxygen partial pressures, which were calculated from the measured oxygen/nitrogen flows, assuming a constant environmental pressure of 1000 mbar. To obtain the Stern−Volmer Plot (SVP), all the measurements were made at 10 different oxygen partial pressures between 0 and 0.1 bar and a room temperature of 21 °C.

■ ASSOCIATED CONTENT

Supporting Information

Additional details on synthesis, characterization, and theoretical calculations; additional figures for oxygen sensing; and cif files. This material is available free of charge via the Internet at http://pubs.acs.org.

AUTHOR INFORMATION

Corresponding Author

*J.F.F.-S.: e-mail jffernan@ugr.es. E.B.: e-mail e.baranoff@bham.ac.uk.

Notes

The authors declare no competing financial interest.

ACKNOWLEDGMENTS

We acknowledge financial support for this work by the Regional Government of Andalusia (Excellence projects P07-FQM-2625 and P07-FQM-2738), the Spanish Ministry of Science and Innovation (CTQ2008-01394), Solvay S.A., and the Swiss National Science Foundation (NCCR-MUST interdisciplinary research program). M.M.S. thanks the Regional Government of Andalusia for supporting her doctoral grant.

REFERENCES

(1) Wolfbeis, O. S. *J. Mater. Chem.* **2005**, *15*, 2657.
(2) Amao, Y. *Microchim. Acta* **2003**, *143*, 1.
(3) Loloee, R.; Askeland, P. A.; Ghosh, R. N. In *Dissolved Oxygen Sensing in a Flow Stream using Molybdenum Chloride Optical Indicators*, Sensors, 2007 IEEE, 28−31 Oct. 2007, 2007; 2007; p 1404.
(4) Baleizao, C.; Nagl, S.; Schäferling, M.; Berberan-Santos, M. N.; Wolfbeis, O. S. *Anal. Chem.* **2008**, *80*, 6449.
(5) Achatz, D. E.; Meier, R. J.; Fischer, L. H.; Wolfbeis, O. S. *Angew. Chem., Int. Ed.* **2011**, *50*, 260.
(6) Lange, C. A. K.; Stavrakas, P.; Luhmann, U. F. O.; de Silva, D. J.; Ali, R. R.; Gregor, Z. J.; Bainbridge, J. W. B. *Am. J. Ophthalmol.* **2011**, *152*, 406.
(7) Song, D. H.; Kim, H. D.; Kim, K. C. *Optics Lasers Eng.* **2012**, *50*, 74.
(8) Xie, K.; Zhang, X.-W.; Huang, L.; Wang, Y.-T.; Lei, Y.; Rong, J.; Qian, C.-W.; Xie, Q.-L.; Wang, Y.-F.; Hong, A.; Xiong, S. *Cytotechnology* **2011**, *63*, 345.
(9) Medina-Castillo, A. L.; Fernández-Sánchez, J. F.; Fernández-Gutiérrez, A. *Adv. Funct. Mater.* **2011**, *21*, 3488.
(10) Liu, Z.; Bian, Z.; Huang, C.; Bozec, H.; Guerchais, V. In *Luminescent Iridium Complexes and Their Applications Molecular Organometallic Materials for Optics*; Springer: Berlin/Heidelberg, 2010; Vol. *28*, p 113.
(11) Ruggi, A.; van Leeuwen, F. W. B.; Velders, A. H. *Coord. Chem. Rev.* **2011**, *255*, 2542.
(12) Koren, K.; Borisov, S. M.; Saf, R.; Klimant, I. *Eur. J. Inorg. Chem.* **2011**, *2011*, 1531.
(13) Amao, Y.; Ishikawa, Y.; Okura, I. *Anal. Chim. Acta* **2001**, *445*, 177.
(14) Fernández-Sánchez, J. F.; Cannas, R.; Spichiger, S.; Steiger, R.; Spichiger-Keller, U. E. *Anal. Chim. Acta* **2006**, *566*, 271.
(15) Fernández-Sánchez, J. F.; Roth, T.; Cannas, R.; Nazeeruddin, M. K.; Spichiger, S.; Graetzel, M.; Spichiger-Keller, U. E. *Talanta* **2007**, *71*, 242.
(16) Marin-Suarez del Toro, M.; Fernandez-Sanchez, J. F.; Baranoff, E.; Nazeeruddin, M. K.; Graetzel, M.; Fernandez-Gutierrez, A. *Talanta* **2010**, *82*, 620.
(17) Medina-Castillo, A. L.; Fernandez-Sanchez, J. F.; Klein, C.; Nazeeruddin, M. K.; Segura-Carretero, A.; Fernandez-Gutierrez, A.; Graetzel, M.; Spichiger-Keller, U. E. *Analyst* **2007**, *132*, 929.
(18) Borisov, S.; Seifner, R.; Klimant, I. *Anal. Bioanal. Chem.* **2011**, *400*, 2463.
(19) Lu, H.; Jin, Y.; Tian, Y.; Zhang, W.; Holl, M. R.; Meldrum, D. R. *J. Mater. Chem.* **2011**, *21*, 19293.
(20) Evans, R. C.; Douglas, P. *Anal. Chem.* **2006**, *78*, 5645.
(21) Hansch, C.; Leo, A.; Taft, R. W. *Chem. Rev.* **1991**, *91*, 165.
(22) Baranoff, E.; Curchod, B. F. E.; Monti, F.; Steimer, F.; Accorsi, G.; Tavernelli, I.; Rothlisberger, U.; Scopelliti, R.; Grätzel, M.; Nazeeruddin, M. K. *Inorg. Chem.* **2012**, *51*, 799.
(23) Yang, J.-S.; Liu, K.-T.; Su, Y. O. *J. Phys. Org. Chem.* **1990**, *3*, 723.
(24) Kessler, F.; Costa, R. D.; Di Censo, D.; Scopelliti, R.; Ortì, E.; Bolink, H. J.; Meier, S.; Sarfert, W.; Grätzel, M.; Nazeeruddin, M. K.; Baranoff, E. *Dalton Trans.* **2012**, *41*, 180.
(25) Baranoff, E.; Jung, I.; Scopelliti, R.; Solari, E.; Grätzel, M.; Nazeeruddin, M. K. *Dalton Trans.* **2011**, *40*, 6860.
(26) Li, J.; Djurovich, P. I.; Alleyne, B. D.; Yousufuddin, M.; Ho, N. N.; Thomas, J. C.; Peters, J. C.; Bau, R.; Thompson, M. E. *Inorg. Chem.* **2005**, *44*, 1713.
(27) Demas, J. N.; DeGraff, B. A. *Sens. Actuators, B* **1993**, *11*, 35.
(28) Lehrer, S. *Biochemistry* **1971**, *10*, 3254.
(29) Di Marco, G.; Lanza, M. *Sens. Actuators, B* **2000**, *63*, 42.
(30) Mills, A. *Analyst* **1998**, *123*, 1135.
(31) Papkovsky, D. B.; Mohr, G. J.; Wolfbeis, O. S. *Anal. Chim. Acta* **1997**, *337*, 201.
(32) Fernández-Sánchez, J. F.; Nezel, T.; Steiger, R.; Spichiger-Keller, U. E. *Sens. Actuators, B* **2006**, *113*, 630.
(33) Rojas-Graü, M. A.; Oms-Oliu, G.; Soliva-Fortuny, R.; Martín-Belloso, O. *Int. J. Food Sci. Technol.* **2009**, *44*, 875.
(34) Denison, D. M.; Ernsting, J.; Tonkins, W. J.; Cresswell, A. W. *Nature* **1968**, *218*, 1110.
(35) Kimyonok, A.; Domercq, B.; Haldi, A.; Cho, J.-Y.; Carlise, J. R.; Wang, X.-Y.; Hayden, L. E.; Jones, S. C.; Barlow, S.; Marder, S. R.; Kippelen, B.; Weck, M. *Chem. Mater.* **2007**, *19*, 5602.
(36) Shen, J.; Snook, R. D. *Chem. Phys. Lett.* **1989**, *155*, 585.
(37) Duisenberg, A. J. M.; Kroon-Batenburg, L. M. J.; Schreurs, A. M. M. *J. Appl. Crystallogr.* **2003**, *36*, 220.
(38) Blessing, R. H. *Acta Crystallogr., Sect. A: Found. Crystallogr.* **1995**, *51*, 33.
(39) Sheldrick, G. M. *Acta Crystallogr., Sect. A: Found. Crystallogr.* **2008**, *64*, 112.
(40) Spek, A. L. *Acta Crystallogr., Sect D: Biol. Crystallogr.* **2009**, *65*, 148.
(41) Zhao, Y.; Truhlar, D. G. *Theor. Chem. Acc.* **2008**, *120*, 215.
(42) Hay, P. J.; Wadt, W. R. *J. Chem. Phys.* **1985**, *82*, 299.
(43) Schaefer, A.; Horn, H.; Ahlrichs, R. *J. Chem. Phys.* **1992**, *97*, 2571.
(44) Schaefer, A.; Huber, C.; Ahlrichs, R. *J. Chem. Phys.* **1994**, *100*, 5829.
(45) Frisch, M. J.; Trucks, G. W.; Schlegel, H. B.; Scuseria, G. E.; Robb, M. A.; Cheeseman, J. R.; Scalmani, G.; Barone, V.; Mennucci, B.; Petersson, G. A.; Nakatsuji, H.; Caricato, M.; Li, X.; Hratchian, H. P.; Izmaylov, A. F.; Bloino, J.; Zheng, G.; Sonnenberg, J. L.; Hada, M.; Ehara, M.; Toyota, K.; Fukuda, R.; Hasegawa, J.; Ishida, M.; Nakajima, T.; Honda, Y.; Kitao, O.; Nakai, H.; Vreven, T.; Montgomery, J. A., Jr.; Peralta, J. E.; Ogliaro, F.; Bearpark, M.; Heyd, J. J.; Brothers, E.; Kudin, K. N.; Staroverov, V. N.; Kobayashi, R.; Normand, J.; Raghavachari, K.; Rendell, A.; Burant, J. C.; Iyengar, S. S.; Tomasi, J.; Cossi, M.; Rega, N.; Millam, J. M.; Klene, M.; Knox, J. E.; Cross, J. B.; Bakken, V.; Adamo, C.; Jaramillo, J.; Gomperts, R.; Stratmann, R. E.; Yazyev, O.; Austin, A. J.; Cammi, R.; Pomelli, C.; Ochterski, J. W.; Martin, R. L.; Morokuma, K.; Zakrzewski, V. G.; Voth, G. A.; Salvador, P.; Dannenberg, J. J.; Dapprich, S.; Daniels, A. D.; Farkas, Ö.; Foresman, J. B.; Ortiz, J. V.; Cioslowski, J.; Fox, D. J. *Gaussian 09, Revision A.02*; Gaussian, Inc.: Wallingford, CT, 2009.
(46) Tomasi, J.; Mennucci, B.; Cammi, R. *Chem. Rev.* **2005**, *105*, 2999.
(47) Swiderek, K.; Paneth, P. *J. Phys. Org. Chem.* **2009**, *22*, 845.
(48) Zhao, Y.; Schultz, N. E.; Truhlar, D. G. *J. Chem. Theory Comput.* **2006**, *2*, 364.